J. Mech. Phys. Solids 206 (2026) 106385

Contents lists available at ScienceDirect

Journal of the Mechanics and Physics of Solids

journal homepage: www.elsevier.com/locate/jmps

Exceptional points and chiral mode conversion in non-Hermitian elastic media

Youdong Duan [a], Linlin Geng [a], Guoliang Huang [b,*], Xiaoming Zhou [a,*]

[a] Key Laboratory of Dynamics and Control of Flight Vehicle of Ministry of Education, School of Aerospace Engineering, Beijing Institute of Technology, Beijing 100081, PR China

[b] Department of Mechanics and Engineering Science, Peking University, Beijing 100871, PR China

ARTICLE INFO

Keywords:
Non-Hermitian system
Exceptional point
Elastic waves
Anisotropic elastic media
Chiral mode conversion

ABSTRACT

Non-Hermitian behaviors for elastic waves, including the parity-time (PT) symmetric and anti-PT symmetric exceptional points (EPs) as well as chiral mode conversion via the dynamic encircling of them, are realized in a unified model based on anisotropic elastic media with complex modulus. Based on the tight-binding approximation of elastodynamic equations, the coupling interaction between elastic wave modes is described by the non-Hermitian Hamiltonian, which is used to derive the existence condition of PT-symmetric and anti-PT-symmetric EPs in different parameter systems. Eigenmode evolution of elastic waves in the process of dynamic encircling of EPs is studied in the spatially modulated model consisting of the multilayered anisotropic media. Chiral mode conversion for elastic waves as dominated by the encircling direction is disclosed by the developed model. The dynamical encircling of a PT-symmetric EP can lead to chiral mode conversion for the symmetric phase, while encircling an anti-PT-symmetric EP results in chiral mode switching for the broken phase. Dynamic evolution along regular and irregular paths are analyzed to demonstrate the topological robustness of chiral mode conversion.

1. Introduction

Nonconservative systems are open systems that could interact with the external environment. They generally possess complex-valued eigenvalues and non-orthogonal eigenvectors, which dramatically distinguish themselves from conservative systems. Non-conservative systems can be characterized by non-Hermitian Hamiltonians when formulated in the Schrödinger-like equation framework. The classical-quantum analogy can thus be established, providing an innovative perspective for exploiting anomalous wave control (Christensen et al., 2024). Exceptional point (EP), at which eigenvalues and eigenvectors coalesce simultaneously, is the landmark signature of non-Hermitian systems, and has been observed in various physical platforms ranging from quantum-mechanical (Naghiloo et al., 2019), photonic (Li et al., 2023), electromagnetic (Koutserimpas and Fleury, 2020), to acoustic/elastic wave systems (Gu et al., 2021). Through the careful balancing of the energy gain and loss, these systems can exhibit the parity-time (PT) symmetry and spontaneous symmetry-broken phase transition. Novel wave phenomena associated to EPs have been found, including unidirectional reflectionless propagation (Fleury et al., 2015; Wu et al., 2019), super-sensitivity (Xing et al., 2020), coherent perfect absorption and lasing (Cai et al., 2023), etc. The Riemann topology structure near EPs in a parameter space is another peculiar behavior of non-Hermitian systems (Ding et al., 2022; Yang et al., 2017). The eigenmode, when adiabatically encircling an EP in one complete cycle, will be flipped instead of recovering to itself (Dembowski et al., 2001, 2004; Gao et al.,

* Corresponding authors.
E-mail addresses: guohuang@pku.edu.cn (G. Huang), zhxming@bit.edu.cn (X. Zhou).

https://doi.org/10.1016/j.jmps.2025.106385
Received 30 May 2025; Received in revised form 16 September 2025; Accepted 29 September 2025
Available online 1 October 2025

2015). When dynamically (non-adiabatically) encircling an EP, the eigenmode would undergo the chiral switching with the ending state that is up to the encircling direction, while irrelevant to the beginning state, as demonstrated in quantum-mechanical (Liu et al., 2021b), optical (Zhang et al., 2018, 2019; Liu et al., 2021a; Feng and Sun, 2022; Liu et al., 2022; Wei et al., 2022; Li et al., 2020), and mechanical systems (Geng et al., 2021a,b).

Acoustic waves support only the non-shear dilatational mode, and a pure acoustic mode can be captured by an enclosed cavity with rigid boundaries. Thanks to the design flexibility for the cavity coupling and acoustic gain/loss modulation, more complex EP phenomena have been discovered, including anisotropic EP (Ding et al., 2018), higher-order EP (Ding et al., 2016), and exceptional nexus (Tang et al., 2020), accompanied by richer eigenvalue topological patterns. The evolution dynamics of eigenmodes enclosing the EP have also been deeply explored in acoustic platforms. The adiabatic evolution can be implemented in isolated element structures which is designed according to parametric points distributed in the loop around the EP (Ding et al., 2016). To realize the dynamic evolution, different acoustic elements are coupled together to ensure the appearance of non-adiabatic transition in the space-driven dynamic encircling of EPs (Duan et al., 2023). The dynamic encircling of an anti-PT-symmetric EP is also attainable, but engineered in a more complicated system. A three-state system hosted by three coupled waveguides is firstly constructed, and then the intermediate state with high loss is adiabatically eliminated such that the anti-PT-symmetric EP can be formed in an effective two-state system (Duan et al., 2024). The dynamic encircling of the PT-symmetric EP can lead to acoustic chiral transfer of symmetry-phase modes. By contrast, the dynamic encircling of the anti-PT-symmetric EP would result in the chiral switching of symmetry-broken states, which may receive more interests because the energy of symmetry-broken eigenmodes is localized in individual waveguides, which can be used directly as input and output channels.

Waves in elastic media possess rich polarization modes and complicated mode couplings compared with acoustic waves. The complexity of elastic systems provides a large degree for manipulating the non-Hermitian elastodynamic behavior as explored in time-varying elastic media (Torrent et al., 2018; Nassar et al., 2017, 2020), odd elasticity/density media (Chen et al., 2021; Gao et al., 2022; Wu et al., 2023), and complex modulus media (Li and Wang, 2023). The energy gain/loss modulation in an elastic continuum can be implemented by coupling the medium system with external physical fields to produce non-conservative energy transfer. For example, the energy loss modulation in elastic medium can be achieved by integrating the ferromagnetic/ferroelectric particles into an elastomer, which are driven by external magnetic or electric fields (Borin and Stepanov, 2015). The other approach, particularly effective for the gain design, can be inspired from the implementation of lattice metamaterials composed of composite piezoelectric structures (Singh et al., 2021, 2022). Their constitutive elements typically incorporate hybrid elastic and piezoelectric materials connected with shunting circuits, which are arranged in a certain lattice periodicity. In the long-wavelength regime, these lattice metamaterials can be homogenized into nonconservative elastic continua, and the non-Hermitian gain effect can be acquired by the active circuit design. Potential applications of non-Hermitian elastic waves consist of non-reciprocal energy transport (Elbaz et al., 2022), non-Hermitian skin effect (Wu et al., 2024) and ultra-sensitivity sensing (Xing et al., 2020; Yuan et al., 2022). In elastic wave systems, the PT-symmetric EP has been widely explored, and can be categorized into the resonance EP (Cai et al., 2022; Jin et al., 2024; Thomes et al., 2024) and non-resonance EP (Li and Wang, 2023; Fishman et al., 2024), which are associated with the eigenvalue problem in the frequency and wavenumber domain, respectively. The resonance EP can be constructed in the gain–loss balanced piezoelectric beam with shunt circuit, and used for the unidirectional cloaking and highly sensitive sensing (Cai et al., 2023). The non-resonance EP can be created in bi-layer elastic media, and exhibits the frozen mode with anomalous scattering of unitary transmission (Fishman et al., 2024). The evolution dynamics of elastic waves enclosing the EP were rarely explored. Elastic laminate structure can act as an energy source or sink by encircling the non-resonance EP (Elbaz et al., 2022). However, the dynamic encircling of the EP is only available in selective cases for forward and backward Bloch waves, where the chiral dynamics cannot be fully identified.

The anisotropic-elasticity media include various types of polarization modes, and support the strong mode coupling in the presence of complex-valued elastic constants. This makes anisotropic elastic media a significant platform to explore the non-Hermitian behavior for elastic waves. In this work, we report the observation of PT-symmetric and anti-PT-symmetric EPs for elastic waves in a unified model based on anisotropic elastic media with complex modulus. Furthermore, the chiral mode conversion of elastic waves is demonstrated through the dynamic encircling of EPs. In Section 2, the wave equation and coupled-mode model are established to characterize elastic wave propagation in two-dimensional anisotropic media. The existence conditions of PT-symmetric and anti-PT-symmetric EPs of elastic waves are derived from the eigenvalue analysis in the wavenumber domain. In Section 3, the spatially modulated model consisting of the multilayered structure is developed to implement the dynamic encircling of EPs, and demonstrate the chiral transfer for symmetric-phase and symmetry-broken modes of elastic waves. The conclusions are outlined in Section 4.

2. EP behavior in anisotropic elastic media

2.1. Wave equation and eigenvalue problem

Consider a two-dimensional (2D) elastic medium with the general anisotropic elasticity in the plane-strain state. In Cartesian coordinates (x, y), the constitutive equation is written in Voigt notation as

$$\hat{\boldsymbol{\sigma}} = \hat{\mathbf{C}}\hat{\boldsymbol{\varepsilon}}, \quad \hat{\mathbf{C}} = \begin{bmatrix} C_{11} & C_{12} & C_{16} \\ C_{12} & C_{22} & C_{26} \\ C_{16} & C_{26} & C_{66} \end{bmatrix} \tag{1}$$

where the vectors of stress and strain are $\hat{\boldsymbol{\sigma}} = \left[\sigma_x, \sigma_y, \tau_{xy}\right]^{\mathrm{T}}$ and $\hat{\boldsymbol{\varepsilon}} = \left[\varepsilon_x, \varepsilon_y, \gamma_{xy}\right]^{\mathrm{T}}$. The mass density and displacement vector are denoted by ρ and $\mathbf{u} = \left[u_x, u_y\right]^{\mathrm{T}}$, respectively. In the time-harmonic case of angular frequency ω, the displacement field follows $\mathbf{u} = \mathbf{U}e^{i\omega t}$ where $\mathbf{U} = \left[U_x, U_y\right]^{\mathrm{T}}$. Consider a plane elastic wave traveling in the positive x direction with the wave vector $\mathbf{k} = k\mathbf{e}_x$. Then we have $\mathbf{U} = \boldsymbol{\Psi}e^{-ikx}$ with $\boldsymbol{\Psi} = \left[\Psi_x, \Psi_y\right]^{\mathrm{T}}$. The elastodynamic equation of this 2D anisotropic medium is expressed as

$$\begin{cases} C_{11}\dfrac{\partial^2 u_x}{\partial x^2} + C_{16}\dfrac{\partial^2 u_y}{\partial x^2} = \rho\dfrac{\partial^2 u_x}{\partial t^2} \\ C_{16}\dfrac{\partial^2 u_x}{\partial x^2} + C_{66}\dfrac{\partial^2 u_y}{\partial x^2} = \rho\dfrac{\partial^2 u_y}{\partial t^2} \end{cases} \tag{2}$$

or alternatively

$$\left(\boldsymbol{\Gamma} - \frac{\rho\omega^2}{k^2}\mathbf{I}\right)\begin{bmatrix} \Psi_x \\ \Psi_y \end{bmatrix} = \mathbf{0}, \quad \boldsymbol{\Gamma} = \begin{bmatrix} C_{11} & C_{16} \\ C_{16} & C_{66} \end{bmatrix} \tag{3}$$

where $\boldsymbol{\Gamma}$ is known as the Christoffel matrix, and $\mathbf{I}$ is the identity matrix of rank two. The eigenvalue (wave velocity) and eigenvector (polarization mode) can be obtained by solving the eigenvalue problem of Eq. (3). In the isotropic case ($C_{16} = 0$), eigenvalue solutions are given by

$$\begin{cases} (\omega/k)_{\mathrm{L}} = \sqrt{C_{11}/\rho}, \quad \boldsymbol{\Psi}_{\mathrm{L}} = [1, 0]^{\mathrm{T}} \\ (\omega/k)_{\mathrm{T}} = \sqrt{C_{66}/\rho}, \quad \boldsymbol{\Psi}_{\mathrm{T}} = [0, 1]^{\mathrm{T}} \end{cases} \tag{4}$$

Eq. (4) characterizes the velocity and polarization properties of longitudinal and transverse waves. Two velocity eigenvalues can be degenerate if $C_{11} = C_{66}$, but their wave modes are always orthogonal, signifying the Hermitian nature.

In the anisotropic case with $C_{16} \neq 0$, eigenvalue solutions are given by

$$(\omega/k)_{\pm}^2 = \frac{C_{11} + C_{66} \pm \sqrt{\left(C_{11} - C_{66}\right)^2 + 4C_{16}^2}}{2\rho}, \quad \boldsymbol{\Psi}_{\pm} = \left[\frac{C_{11} - C_{66} \pm \sqrt{\left(C_{11} - C_{66}\right)^2 + 4C_{16}^2}}{2C_{16}}, 1\right]^{\mathrm{T}} \tag{5}$$

According to Eq. (5), the EP at which eigenvalues and eigenvectors coalesce simultaneously appears on the condition of

$$\left(C_{11} - C_{66}\right)^2 + 4C_{16}^2 = 0 \tag{6}$$

The EP condition indicated by Eq. (6) requires elastic constants to be complex values, dictating that the EP-supported media are nonconservative systems associated with the energy gain and loss.

2.2. Coupled-mode model

Introduce the dimensionless coordinate $\zeta = k_{\mathrm{s}}x$ with $k_{\mathrm{s}} = \omega\sqrt{\rho/C_{66}}$. The displacement field can be rewritten as $\mathbf{U} = \boldsymbol{\Psi}e^{-i\eta\zeta}$, where $\eta = k/k_{\mathrm{s}}$ is the dimensionless wavenumber. The equivalent form of Eq. (2) is given by

$$\begin{cases} \dfrac{\partial^2 U_x}{\partial \zeta^2} = \beta_1 U_x(\zeta) + \kappa U_y(\zeta) \\ \dfrac{\partial^2 U_y}{\partial \zeta^2} = \kappa U_x(\zeta) + \beta_2 U_y(\zeta) \end{cases} \tag{7}$$

where the normalized parameters β_1, β_2, and κ are defined by

$$\beta_1 = \frac{C_{66}^2}{C_{16}^2 - C_{11}C_{66}}, \quad \beta_2 = \frac{C_{11}C_{66}}{C_{16}^2 - C_{11}C_{66}}, \quad \kappa = -\frac{C_{16}C_{66}}{C_{16}^2 - C_{11}C_{66}} \tag{8}$$

Eq. (7) is further expressed as

$$\left(\mathbf{K} - \eta^2\mathbf{I}\right)\begin{bmatrix} \Psi_x \\ \Psi_y \end{bmatrix} = \mathbf{0}, \quad \mathbf{K} = \begin{bmatrix} -\beta_1 & -\kappa \\ -\kappa & -\beta_2 \end{bmatrix} \tag{9}$$

Eigenvalue solutions to Eq. (9) are given by

$$\eta_{\pm}^2 = -\frac{\beta_1 + \beta_2 \pm \sqrt{\left(\beta_1 - \beta_2\right)^2 + 4\kappa^2}}{2}, \quad \boldsymbol{\Psi}_{\pm} = \left[\frac{\beta_1 - \beta_2 \pm \sqrt{\left(\beta_1 - \beta_2\right)^2 + 4\kappa^2}}{2\kappa}, 1\right]^{\mathrm{T}} \tag{10}$$

According to Eq. (10), the condition for simultaneous degeneracy of eigenvalues and eigenvectors is given by

$$\left(\beta_1 - \beta_2\right)^2 + 4\kappa^2 = 0 \tag{11}$$

which is the dimensionless form of the EP condition (6).

In what follows, the tight-binding approximation will be adopted to simplify Eq. (9) such that the elastodynamic equation can be formulated in the form of the Schrödinger-like equation characterized by a non-Hermitian Hamiltonian. The tight-binding model originates from solid-state physics (Harrison, 1994), and it applies in the scenario that the system response is dominated by isolated states with weak couplings. Here, we focus on two fundamental states supported by 2D anisotropic elastic medium, namely longitudinal and transverse polarization dominated modes, and consider the case that their couplings are weak such that the tight-binding model can be applied to the studied system. According to the tight-binding approximation, the elastic medium is considered as an undisturbed system superimposed with small perturbations. The undisturbed system comprises the longitudinal and transverse polarization modes having nearly identical wavevectors, i.e., $|\beta_1| \approx |\beta_2|$. Meanwhile, the coupling between two modes as characterized by κ is seen as a small perturbation, satisfying $|\kappa| \ll |\beta_{1,2}|$. These dimensionless parameters, $\beta_{1,2}$ and κ, are related to modulus parameters by Eq. (8). Therefore, the tight-binding approximation ($|\kappa| \ll |\beta_1| \approx |\beta_2|$) is equivalent to the modulus condition $|C_{16}| \ll |C_{11}| \approx |C_{66}|$. Notice that this tight-binding condition should be satisfied at both EPs and loop trajectory enclosing them such that the coupled-mode description can be used to implement the design of chiral mode conversion. Based on above approximation, the eigenvalue of the medium system can be represented by $\eta = 1 + \delta$, where the parameter δ satisfies $|\delta| \ll 1$, and it denotes the small disturbance of eigenvalues with respect to the unperturbed system. Accordingly, there exists the approximate relation $\eta^2 \approx 1 + 2\delta$. Substitute this relation into Eq. (9), obtaining the δ-eigenvalue governed equation

$$\mathbf{H}_{\mathrm{p}}\boldsymbol{\Psi} = \delta\boldsymbol{\Psi}, \quad \mathbf{H}_{\mathrm{p}} = \frac{1}{2}\begin{bmatrix} -\beta_1 - 1 & -\kappa \\ -\kappa & -\beta_2 - 1 \end{bmatrix} \tag{12}$$

The Hamiltonian of the undisturbed system is described by the identity matrix $\mathbf{I}$. Thereby, the eigenvalue equation of the medium system can be arranged as a generic tight-binding form

$$\mathbf{H}_{\mathrm{total}}\boldsymbol{\Psi} = \eta\boldsymbol{\Psi}, \quad \mathbf{H}_{\mathrm{total}} = \mathbf{I} + \mathbf{H}_{\mathrm{p}} = \frac{1}{2}\begin{bmatrix} 1 - \beta_1 & -\kappa \\ -\kappa & 1 - \beta_2 \end{bmatrix} \tag{13}$$

Based on the Hamiltonian matrix $\mathbf{H}_{\mathrm{total}}$, the spatial coupled-mode equation of the anisotropic medium is constructed as

$$i\frac{\mathrm{d}}{\mathrm{d}\zeta}\tilde{\mathbf{U}} = \mathbf{H}_{\mathrm{total}}\tilde{\mathbf{U}} \tag{14}$$

where $\tilde{\mathbf{U}}$ is introduced satisfying $\mathbf{U} = \left(\tilde{\mathbf{U}} + \tilde{\mathbf{U}}^*\right)/2$ with the star symbol denoting the complex conjugate operation. Solutions to the eigenvalue problem of Eq. (13) are given by

$$\eta_{\mp}^{\mathrm{TB}} = \frac{2 - \left(\beta_1 + \beta_2\right) \mp \sqrt{\left(\beta_1 - \beta_2\right)^2 + 4\kappa^2}}{4}, \quad \boldsymbol{\Psi}_{\pm}^{\mathrm{TB}} = \left[\frac{\beta_1 - \beta_2 \pm \sqrt{\left(\beta_1 - \beta_2\right)^2 + 4\kappa^2}}{2\kappa}, 1\right]^{\mathrm{T}} \tag{15}$$

It is seen from Eq. (15) that the coupled-mode model delivers the same EP condition as Eq. (11), thus can capture fundamental properties of the EP behavior in terms of the Hamiltonian equation framework. Although the tight-binding approximation is assumed, it would be demonstrated later that elastic systems can still support the chiral mode conversion behavior. Importantly, the tight-binding model can offer deep insights towards the understanding and construction of the system symmetry and chiral dynamics induced by encircling EPs. Notice that the tight-binding model may deviate significantly from the original model when the condition $|C_{16}| \ll |C_{11}| \approx |C_{66}|$ is strongly violated.

To proceed, there are two options for the medium system to fulfill the EP condition (6). One option is to introduce the complex modulus $C_{11} = C_{11}' + iC_{11}''$, while keep C_{66} and C_{16} being real values, and the medium system would support PT-symmetric EPs, as examined in Section 2.3. The other option is to introduce the complex modulus $C_{16} = C_{16}' + iC_{16}''$, while C_{11} and C_{66} are real values. In this case, the medium system supports anti-PT-symmetric EPs as disclosed in Section 2.4.

2.3. PT-symmetric EPs

Consider the case that C_{11} is the complex-valued modulus. The Hamiltonian matrix $\mathbf{H}_{\mathrm{total}}$ is expressed as

$$\mathbf{H}_{\mathrm{total}} = \frac{1}{2C_{11}'}\begin{bmatrix} C_{11}' + C_{66} - iC_{11}''C_{66}/C_{11}' & -C_{16} \\ -C_{16} & 2C_{11}' \end{bmatrix} \tag{16}$$

According to Eq. (6), the EP condition is summarized as $C_{11}' = C_{66}$ and $C_{11}'' = \pm 2C_{16}$. Now substitute the relation $C_{11}' = C_{66}$ into the Hamiltonian matrix $\mathbf{H}_{\mathrm{total}}$. The coupled-mode equation (14) is rewritten as

$$i\frac{\mathrm{d}}{\mathrm{d}\zeta}\tilde{\mathbf{U}} = \mathbf{H}_{\mathrm{total}}\tilde{\mathbf{U}}, \quad \mathbf{H}_{\mathrm{total}} = \frac{1}{2C_{66}}\begin{bmatrix} 2C_{66} - iC_{11}'' & -C_{16} \\ -C_{16} & 2C_{66} \end{bmatrix} \tag{17}$$

Perform the gauge transformation $\boldsymbol{\Phi} = \tilde{\mathbf{U}}\exp[C_{11}''\zeta/(4C_{66})]$ for Eq. (17), giving rise to

$$i\frac{\mathrm{d}}{\mathrm{d}\zeta}\boldsymbol{\Phi} = \mathbf{H}_{\mathrm{PT}}\boldsymbol{\Phi}, \quad \mathbf{H}_{\mathrm{PT}} = \frac{1}{4C_{66}}\begin{bmatrix} 4C_{66} - iC_{11}'' & -2C_{16} \\ -2C_{16} & 4C_{66} + iC_{11}'' \end{bmatrix} \tag{18}$$

It can be found that the Hamiltonian matrix $\mathbf{H}_{\mathrm{PT}}$ follows the PT symmetry

$$(\mathcal{PT})\mathbf{H}_{\mathrm{PT}}(\mathcal{PT})^{-1} = \mathbf{H}_{\mathrm{PT}} \tag{19}$$

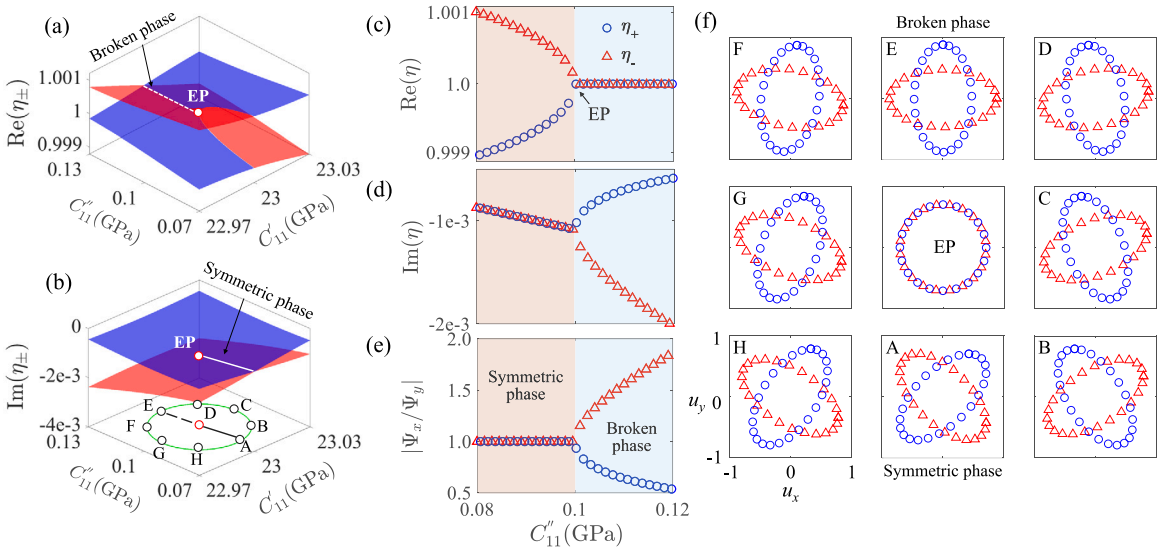

Fig. 1. (a) Real and (b) imaginary parts of eigenvalues $\eta_\pm$ in the parameter space (C'_{11}, C''_{11}) calculated by Eq. (10); (c, d) The eigenvalue and (e) eigenmode amplitude ratio in the line of $C'_{11} = C_{66}$, where $\mathbf{\Psi}_\pm = [\Psi_x, \Psi_y]^{\mathrm{T}}_\pm$; (f) Particle motion trajectories at the EP and eight nearby parametric points.

where the parity operator $\mathcal{P}$ can be characterized by the Pauli matrix$\left[\begin{smallmatrix}0&1\\1&0\end{smallmatrix}\right]$ (Ozdemir et al., 2019), and the time-reversal operator $\mathcal{T}$ returns its conjugate when acting on a Hamiltonian matrix. The eigenvalue solutions of Eq. (18) are given by

$$\eta_\pm^{\mathrm{PT}} = \frac{4C_{66} \pm \sqrt{4C_{16}^2 - C_{11}''^2}}{4C_{66}}, \quad \mathbf{\Psi}_\pm^{\mathrm{PT}} = \left[\frac{iC_{11}'' \pm \sqrt{4C_{16}^2 - C_{11}''^2}}{2C_{16}}, 1\right]^{\mathrm{T}} \tag{20}$$

Eigenvalues and eigenvectors are degenerate simultaneously when $C''_{11} = \pm 2C_{16}$, forming the PT-symmetric EP.

Consider material parameters C_{66} = 23 GPa, C_{16} = 0.05 GPa, and ρ = 5000 kg/m^3. The excitation frequency is set as f = 5 kHz. By calculating Eq. (10), real and imaginary parts of eigenvalues $\eta_\pm$ in the 2D parameter space (C'_{11}, C''_{11}) are displayed in Fig. 1(a, b). For brevity, denote the spectrum sheets with low and high values of $|\mathrm{Im}(\eta_\pm)|$ by the L and H mode, respectively. It is seen from Fig. 1(a, b) that the condition $C'_{11} = C_{66}$ defines the coalescing line, where real or imaginary parts of eigenvalues are partially degenerate. Figs. 1(c-e) show respectively the real and imaginary parts of eigenvalues as well as the amplitude ratio of eigenmodes at the coalescing line. In the line region of $C''_{11} < 2C_{16}$, the imaginary parts of eigenvalues coalesce, while their real parts are split, forming the so called branch cut (Zhang et al., 2018). Further insights can be gained from the eigenvector $\mathbf{\Psi}_\pm^{\mathrm{PT}}$ at this line as given by Eq. (20). It is readily derived that the eigenvector follows the relation $\mathcal{PT}\mathbf{\Psi}_\pm^{\mathrm{PT}} = \sigma_\pm \mathbf{\Psi}_\pm^{\mathrm{PT}}$, where $|\sigma_\pm| = 1$. Therefore, the eigenmode amplitude exhibits the balancing distribution $|\Psi_{+,x}^{\mathrm{PT}}/\Psi_{+,y}^{\mathrm{PT}}| = |\Psi_{-,x}^{\mathrm{PT}}/\Psi_{-,y}^{\mathrm{PT}}| = 1$ for either L or H mode, as evidenced in Fig. 1(e). The wave mode with above features is recognized as the PT-symmetric phase (Ozdemir et al., 2019). In the line region of $C''_{11} > 2C_{16}$, the real parts of eigenvalues coalesce while the imaginary parts are different. In this case, the eigenvector is found to follow $\mathcal{PT}\mathbf{\Psi}_\pm^{\mathrm{PT}} = \chi_\pm \mathbf{\Psi}_\mp^{\mathrm{PT}}$, where $|\chi_\pm| \neq 1$ and $\chi_\pm^* \chi_\mp = 1$. Subsequently, the eigenmode amplitude exhibits an asymmetric distribution satisfying $|\Psi_{-,x}^{\mathrm{PT}}/\Psi_{-,y}^{\mathrm{PT}}| = |\Psi_{+,y}^{\mathrm{PT}}/\Psi_{+,x}^{\mathrm{PT}}| > 1$ as shown in Fig. 1(e), which is the signature of the PT-symmetry-broken phase. Notice that two lines intersect at the point of $C''_{11} = 2C_{16}$ which corresponds to the EP. Particle motion trajectories associated to L and H modes are illustrated in Fig. 1(f) for the EP and eight nearby parametric points distributed evenly in the circular loop of radius 0.02 GPa. The wave motion is typically characterized by the elliptical polarization, and the orientation of the polarization axis varies when the parametric point moves along the loop. At the EP, two waves propagate with the circular polarization of same oscillation magnitudes, demonstrating the degeneracy of eigenvectors.

2.4. Anti-PT-symmetric EPs

In the case of the complex-valued modulus $C_{16} = C'_{16} + iC''_{16}$, the Hamiltonian matrix $\mathbf{H}_{\mathrm{total}}$ is expressed as

$$\mathbf{H}_{\mathrm{total}} = \frac{1}{2C_{11}} \begin{bmatrix} C_{11} + C_{66} & -C'_{16} - iC''_{16} \\ -C'_{16} - iC''_{16} & 2C_{11} \end{bmatrix} \tag{21}$$

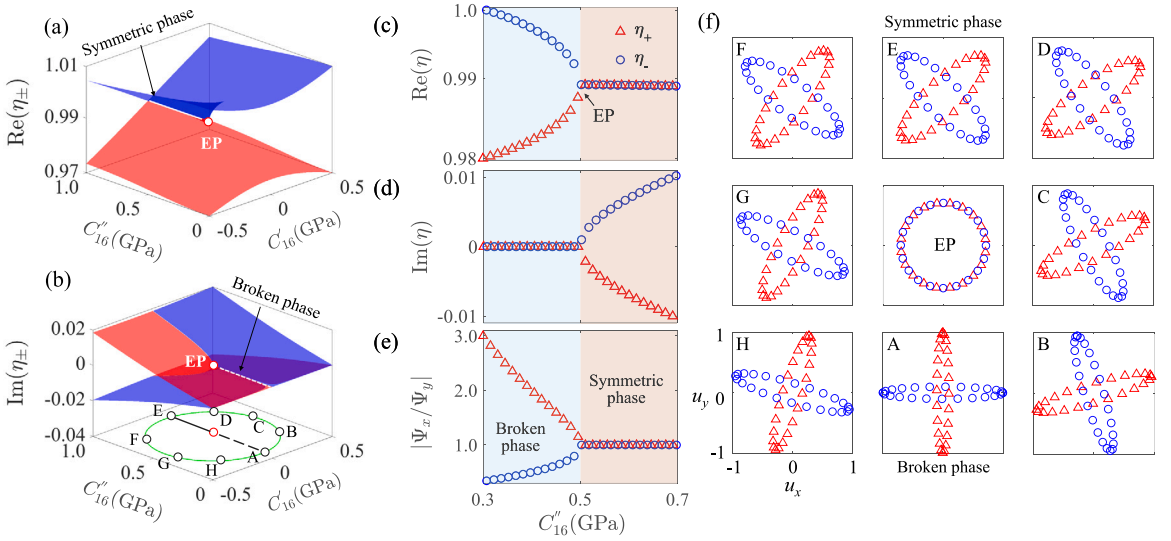

Fig. 2. (a) Real and (b) imaginary parts of eigenvalues $\eta_{\pm}$ in the parameter space (C'_{16}, C''_{16}) calculated by Eq. (10); (c, d) The eigenvalue and (e) eigenmode amplitude ratio in the line of $C'_{16}=0$, where $\mathbf{\Psi}_{\pm}=[\Psi_x,\Psi_y]^{\mathrm{T}}_{\pm}$; (f) Particle motion trajectories at the EP and eight nearby parametric points.

In this case, the EP condition (6) is given by $C'_{16}=0$ and $C''_{16}=\pm\left(C_{11}-C_{66}\right)/2$. By use of the condition $C'_{16}=0$, the coupled-mode equation (14) is simplified as

$$i\frac{\mathrm{d}}{\mathrm{d}\zeta}\tilde{\mathbf{U}}=\mathbf{H}_{\mathrm{total}}\tilde{\mathbf{U}},\quad \mathbf{H}_{\mathrm{total}}=\frac{1}{2C_{11}}\begin{bmatrix} C_{11}+C_{66} & -iC''_{16} \\ -iC''_{16} & 2C_{11}\end{bmatrix} \tag{22}$$

Perform the gauge transformation $\mathbf{\Phi}'=\tilde{\mathbf{U}}\exp[i\zeta(3C_{11}+C_{66})/(4C_{11})]$ for Eq. (22), leading to

$$i\frac{\mathrm{d}}{\mathrm{d}\zeta}\mathbf{\Phi}'=\mathbf{H}_{\mathrm{APT}}\mathbf{\Phi}',\quad \mathbf{H}_{\mathrm{APT}}=\frac{1}{4C_{11}}\begin{bmatrix} C_{66}-C_{11} & -2iC''_{16} \\ -2iC''_{16} & C_{11}-C_{66}\end{bmatrix} \tag{23}$$

Two modes are seen to have the purely imaginary coupling. Now the elastic medium becomes the anti-PT-symmetric system because the Hamiltonian matrix $\mathbf{H}_{\mathrm{APT}}$ follows the anti-PT symmetry

$$(\mathcal{PT})\mathbf{H}_{\mathrm{APT}}(\mathcal{PT})^{-1}=-\mathbf{H}_{\mathrm{APT}} \tag{24}$$

By solving the eigenvalue problem of $\mathbf{H}_{\mathrm{APT}}$, it can be obtained that

$$\eta^{\mathrm{APT}}_{\pm}=\frac{\pm\sqrt{\left(C_{66}-C_{11}\right)^2-4C''^2_{16}}}{4C_{11}},\quad \mathbf{\Psi}^{\mathrm{APT}}_{\pm}=\left[\frac{-i\left(C_{11}-C_{66}\right)\pm i\sqrt{\left(C_{66}-C_{11}\right)^2-4C''^2_{16}}}{2C''_{16}},1\right]^{\mathrm{T}} \tag{25}$$

According to Eq. (25), the anti-PT-symmetric EP is formed when $C''_{16}=\pm(C_{11}-C_{66})/2$.

Consider material parameters $C_{11}=24$ GPa, $C_{66}=23$ GPa, $\rho=5000$ kg/m^3, and the excitation frequency $f=5$ kHz. Eigenvalue results in the parameter space (C'_{16}, C''_{16}) calculated by Eq. (10) are shown in Fig. 2(a, b). It is seen that the coalescing line of eigenvalues appears at $C'_{16}=0$. The imaginary parts of eigenvalues overlap in the line region of $C''_{16}<(C_{11}-C_{66})/2$, as shown in Fig. 2(d). The wave mode in this region is recognized as the symmetry-broken phase because the eigenmode amplitude exhibits an asymmetric distribution as indicated in Fig. 2(e). A deeper understanding can be gained by examining the $\mathcal{PT}$ transformation of the eigenvector $\mathbf{\Psi}^{\mathrm{APT}}_{\pm}$, which results in $\mathcal{PT}\mathbf{\Psi}^{\mathrm{APT}}_{\pm}=\chi_{\pm}\mathbf{\Psi}^{\mathrm{APT}}_{\mp}$ with $|\chi_{\pm}|\neq 1$ and $\chi^{*}_{\pm}\chi_{\mp}=1$, demonstrating the broken-phase behavior. In the line region of $C''_{16}>(C_{11}-C_{66})/2$, the real parts of eigenvalues coalesce as presented in Fig. 2(c). The corresponding eigenvector follows $\mathcal{PT}\mathbf{\Psi}^{\mathrm{APT}}_{\pm}=\sigma_{\pm}\mathbf{\Psi}^{\mathrm{APT}}_{\pm}$ with $|\sigma_{\pm}|=1$, which is the landmark characteristics of the symmetric phase. Thereby, the energy is distributed evenly between two modes as shown in Fig. 2(e). Particle motion trajectories are illustrated in Fig. 2(f), showing similar features as those in the PT-symmetric medium. The particle motion follows the circular trajectory at the EP, while exhibits the elliptical polarization at parametric points on the loop of radius 0.4 GPa around the EP. The orientation of the principle axis changes at different points on the loop, and the aspect ratio of the polarization ellipse varies as well.

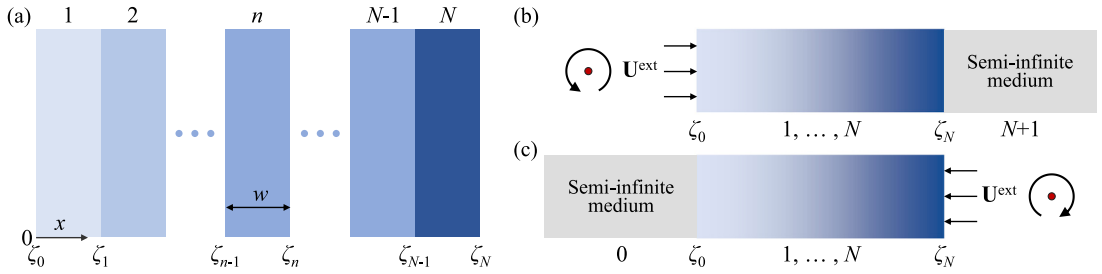

Fig. 3. (a) Schematic of the multilayer structure that supports the dynamic evolution of eigenstates around an EP; The structural systems to implement the mode evolution in the (b) anti-clockwise and (c) clockwise encircling direction.

3. Chiral mode conversion of elastic waves via dynamic encircling of EPs

3.1. Theoretical model

The dynamic encircling of an EP in the 2D parameter space can lead to the chiral mode transfer as demonstrated in acoustic and discrete mechanical systems (Duan et al., 2023, 2024; Geng et al., 2021a,b). These intriguing phenomena will be analyzed for elastic waves in this section. To implement the dynamic encircling of EPs, the loop trajectory is discretized into N parametric points. Now construct a multilayered structure, where each layer is an anisotropic medium of same thickness w and corresponds to a parametric point in the loop, as shown in Fig. 3(a). Elastic wave propagation in the multilayered structure would be equivalent to the dynamic evolution of eigenmodes enclosing the EP. This discretization method allows to study the dynamic evolution of elastic wave modes in an analytical manner, as addressed below.

Elastic wave propagation in the multilayered structure can be formulated based on the transfer matrix method as described below. According to Eq. (7), the wave equation for the n-th layer ($n = 1, \dots, N$) is given by

$$\begin{cases} \dfrac{\partial^2 U_x}{\partial \zeta^2} = \beta_1^{(n)} U_x + \kappa^{(n)} U_y \\ \dfrac{\partial^2 U_y}{\partial \zeta^2} = \kappa^{(n)} U_x + \beta_2^{(n)} U_y \end{cases}, \quad \zeta_{n-1} \leqslant \zeta \leqslant \zeta_n \tag{26}$$

where $\beta_{1,2}^{(n)}$ and $\kappa^{(n)}$ are medium parameters corresponding to the n-th point in the loop. The displacement fields in the n-th layer can be expressed as

$$U_x^{(n)}(\zeta) = \sum_{j=1}^{4} A_j^{(n)} e^{i\eta_j^{(n)}\zeta}, \quad U_y^{(n)}(\zeta) = \sum_{j=1}^{4} M_j^{(n)} A_j^{(n)} e^{i\eta_j^{(n)}\zeta} \tag{27}$$

where $A_j^{(n)}$ are unknown wave amplitudes, and $M_j^{(n)} = -[\beta_1^{(n)} + (\eta_j^{(n)})^2]/\kappa^{(n)}$. For convenience, $\eta_1^{(n)} = -\eta_2^{(n)} = -\eta_+^{(n)}$ and $\eta_3^{(n)} = -\eta_4^{(n)} = -\eta_-^{(n)}$ have been defined, where $\eta_\pm^{(n)}$ denote the eigenvalues of the n-th layer as given by Eq. (10). By substituting Eq. (27) into Eq. (1), the stress fields can be obtained as

$$\begin{cases} \sigma_x^{(n)}(\zeta) = ik_s \left(C_{11}^{(n)} \sum_{j=1}^{4} \eta_j^{(n)} A_j^{(n)} e^{i\eta_j^{(n)}\zeta} + C_{16}^{(n)} \sum_{j=1}^{4} \eta_j^{(n)} M_j^{(n)} A_j^{(n)} e^{i\eta_j^{(n)}\zeta} \right) \\ \tau_{xy}^{(n)}(\zeta) = ik_s \left(C_{16}^{(n)} \sum_{j=1}^{4} \eta_j^{(n)} A_j^{(n)} e^{i\eta_j^{(n)}\zeta} + C_{66} \sum_{j=1}^{4} \eta_j^{(n)} M_j^{(n)} A_j^{(n)} e^{i\eta_j^{(n)}\zeta} \right) \end{cases} \tag{28}$$

Notice that $k_s = \omega\sqrt{\rho/C_{66}}$, where the density ρ and modulus C_{66} are constant values and same for each layer. The n-th layered medium occupies the region of $\zeta_{n-1} \leq \zeta \leq \zeta_n$, where $\zeta_n = nk_s w$. At left and right boundaries of each layer, the state vector $\mathbf{s}^{(n)}(\zeta) = [U_x^{(n)}(\zeta), U_y^{(n)}(\zeta), \sigma_x^{(n)}(\zeta), \tau_{xy}^{(n)}(\zeta)]^{\mathrm{T}}$ satisfy the relation

$$\mathbf{s}^{(n)}\left(\zeta_n\right) = \mathbf{T}^{(n)} \mathbf{s}^{(n)}\left(\zeta_{n-1}\right) \tag{29}$$

where $\mathbf{T}^{(n)}$ is the transfer matrix as given by

$$\mathbf{T}^{(n)} = \mathbf{B}_n \mathbf{R}_n \mathbf{B}_n^{-1}, \quad \mathbf{B}_n = \begin{bmatrix} 1 & 1 & 1 & 1 \\ M_1^{(n)} & M_2^{(n)} & M_3^{(n)} & M_4^{(n)} \\ N_1^{(n)} & N_2^{(n)} & N_3^{(n)} & N_4^{(n)} \\ L_1^{(n)} & L_2^{(n)} & L_3^{(n)} & L_4^{(n)} \end{bmatrix}, \quad \mathbf{R}_n = \mathrm{diag}\left[e^{i\eta_1^{(n)} k_s w}, e^{i\eta_2^{(n)} k_s w}, e^{i\eta_3^{(n)} k_s w}, e^{i\eta_4^{(n)} k_s w} \right] \tag{30}$$

with $N_j^{(n)} = ik_s\eta_j^{(n)}\left(C_{11}^{(n)} + M_j^{(n)}C_{16}^{(n)}\right)$ and $L_j^{(n)} = ik_s\eta_j^{(n)}\left(C_{16}^{(n)} + M_j^{(n)}C_{66}\right)$. The displacement and stress fields are continuous at the interfaces between adjacent layers, leading to the relation $\mathbf{s}^{(m+1)}(\zeta_m) = \mathbf{s}^{(m)}(\zeta_m)$ with $m = 1, \ldots, N-1$. Therefore, the total transfer matrix $\mathbf{T}_{\text{tot}}$ of the multilayered structure follows

$$\mathbf{s}^{(N)}\left(\zeta_N\right) = \mathbf{T}_{\text{tot}}\mathbf{s}^{(1)}\left(\zeta_0\right), \quad \mathbf{T}_{\text{tot}} = \prod_{n=1}^{N}\mathbf{T}^{(N-n+1)} \tag{31}$$

The dynamic evolution of eigenmodes can be analyzed by applying the corresponding displacement excitation $\mathbf{U}^{\text{ext}}$ to the left boundary of the multilayered structure. To minimize the influence of wave scatterings from the end boundary, the multilayered structure is terminated by a semi-infinite medium labeled as the $(N+1)$-th layer, which occupies the region of $\zeta \geq \zeta_N$, as shown in Fig. 3(b). The displacement fields in this layer can be expressed as

$$\begin{cases} U_x^{(N+1)}(\zeta) = A_1^{(N+1)}e^{i\eta_1^{(N+1)}\zeta} + A_3^{(N+1)}e^{i\eta_3^{(N+1)}\zeta} \\ U_y^{(N+1)}(\zeta) = M_1^{(N+1)}A_1^{(N+1)}e^{i\eta_1^{(N+1)}\zeta} + M_3^{(N+1)}A_3^{(N+1)}e^{i\eta_3^{(N+1)}\zeta} \end{cases} \tag{32}$$

where $A_{1,3}^{(N+1)}$ are unknown wave amplitudes. The corresponding stress fields can be computed by Eq. (1). The state vector $\mathbf{s}^{(N+1)}$ at the interface $\zeta = \zeta_N$ of the semi-infinite medium is expressed as

$$\mathbf{s}^{(N+1)}(\zeta_N) = \mathbf{B}_{N+1}\mathbf{R}_{N+1}\mathbf{A}_{N+1} \tag{33}$$

where

$$\mathbf{A}_{N+1} = \begin{bmatrix} A_1^{(N+1)} \\ 0 \\ A_3^{(N+1)} \\ 0 \end{bmatrix}, \quad \mathbf{R}_{N+1} = \text{diag}\left[e^{i\eta_1^{(N+1)}\zeta_N}, e^{i\eta_2^{(N+1)}\zeta_N}, e^{i\eta_3^{(N+1)}\zeta_N}, e^{i\eta_4^{(N+1)}\zeta_N}\right] \tag{34}$$

Denote the stress responses at the excitation boundary ($\zeta = \zeta_0$) by σ_x^{res} and τ_{xy}^{res}, and define the state vector $\mathbf{s}_0 = [U_x^{\text{ext}}, U_y^{\text{ext}}, \sigma_x^{\text{res}}, \tau_{xy}^{\text{res}}]^{\text{T}}$. By use of the continuous condition of displacements and stresses at the interface $\zeta = \zeta_N$, it can be obtained that

$$\mathbf{A}_{N+1} = \left(\mathbf{B}_{N+1}\mathbf{R}_{N+1}\right)^{-1}\mathbf{T}_{\text{tot}}\mathbf{s}_0 \tag{35}$$

Based on Eq. (35), the parameters $A_1^{(N+1)}$, $A_3^{(N+1)}$, σ_x^{res} and τ_{xy}^{res} can be determined. Finally, the displacement fields in the multilayered structure can be analytically computed and used to analyze the mode evolution around the EP.

The dynamic encircling in the opposite direction to the model of Fig. 3(b) can be implemented by terminating the left side of the multilayered structure by a semi-infinite medium labeled as the 0-th layer, and applying the displacement excitation $\mathbf{U}^{\text{ext}}$ to the right boundary ($\zeta = \zeta_N$), as shown in Fig. 3(c). The state vector at the excitation boundary can be defined as $\mathbf{s}_N = [U_x^{\text{ext}}, U_y^{\text{ext}}, \sigma_x^{\text{res}}, \tau_{xy}^{\text{res}}]^{\text{T}}$, where σ_x^{res} and τ_{xy}^{res} are the corresponding stress responses. The displacement fields in the region of $\zeta \leq \zeta_0$ can be expressed as

$$\begin{cases} U_x^{(0)}(\zeta) = A_2^{(0)}e^{i\eta_2^{(0)}\zeta} + A_4^{(0)}e^{i\eta_4^{(0)}\zeta} \\ U_y^{(0)}(\zeta) = M_2^{(0)}A_2^{(0)}e^{i\eta_2^{(0)}\zeta} + M_4^{(0)}A_4^{(0)}e^{i\eta_4^{(0)}\zeta} \end{cases} \tag{36}$$

where $A_{2,4}^{(0)}$ are unknown wave amplitudes. The state vector $\mathbf{s}^{(0)}$ at the interface $\zeta = \zeta_0$ of the semi-infinite medium can be derived as

$$\mathbf{s}^{(0)}(\zeta_0) = \mathbf{B}_0\mathbf{A}_0 \tag{37}$$

where $\mathbf{A}_0 = [0, A_2^{(0)}, 0, A_4^{(0)}]^{\text{T}}$. By use of the continuous conditions at the interface $\zeta = \zeta_0$, it can be obtained that

$$\mathbf{s}_N = \mathbf{T}_{\text{tot}}\mathbf{B}_0\mathbf{A}_0 \tag{38}$$

The displacement fields in the multilayered structure can be calculated by Eq. (38).

3.2. Dynamic encircling of the PT-symmetric EP

The dynamic encircling of the PT-symmetric EP can be implemented by choosing the loop trajectory as drawn in Fig. 4(a), which is parameterized by

$$\begin{cases} C_{11}'(\zeta) = 0.02\cos\left(\omega_r\zeta + \phi_0\right) + 23 \quad \text{(GPa)} \\ C_{11}''(\zeta) = 0.02\sin\left(\omega_r\zeta + \phi_0\right) + 0.1 \quad \text{(GPa)} \end{cases} \tag{39}$$

where $\omega_r = 2\pi/L_t$ and $L_t = Nk_sw$ denotes the total evolution length with $N = 6540$. The modulus $C_{11}^{(n)}$ in the n-th layer ($n = 1, \ldots, N$) is set as $C_{11}(L_n)$, where $L_n = (n-1)k_sw$ and $w = 29.4$ mm, while other material parameters are same as those used in Fig. 1. The property of the terminated semi-infinite medium is chosen according to the rule that its impedance is best matched with the adjacent

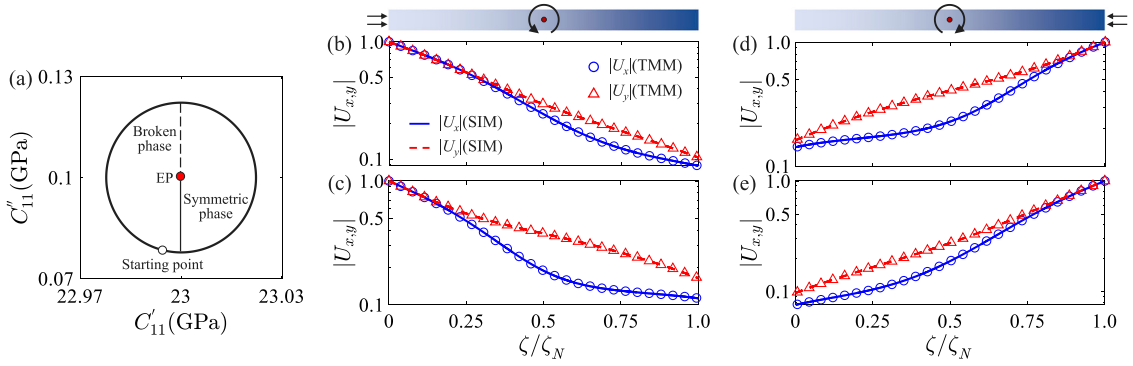

Fig. 4. (a) The circular loop trajectory in the parameter space (C'_{11}, C''_{11}) used for implementing the dynamic encircling of the PT-symmetric EP with the starting point lying near the PT-symmetric phase; Normalized displacement amplitudes in the process of dynamic encircling of the PT-symmetric EP calculated by the transfer-matrix method (TMM) and numerical simulation (SIM) in four cases: (b) the L mode and (c) H mode input for the anti-clockwise evolution; (d) the L mode and (e) H mode input for the clockwise evolution.

layer to minimize the wave reflection from the terminated medium. It can be seen from Fig. 1(a, b) that the modulus parameters fluctuate slightly in the process of dynamic encircling of EPs. Therefore, the semi-infinite medium is set as the same one at the EP, but their imaginary parts are removed because the loss/gain property is not required for reducing wave reflection. According to this rule, the modulus properties of the semi-infinite medium are set as $C_{11} = 23$ GPa, $C_{66} = 23$ GPa, $C_{16} = 0.05$ GPa.

Consider first the case that the starting point is set near the PT-symmetric phase by choosing $\phi_0 = -1.7\pi/3$. The displacement excitation $\mathbf{U}^{\text{ext}}$ is then retrieved from the modal fields at the starting point, and is applied to the left (right) boundary for achieving the anti-clockwise (clockwise) mode evolution along the loop, respectively. Based on the transfer matrix method as presented in Section 3.1, the displacement fields $\mathbf{U}^{(n)}(\zeta)$ in the multilayered structure can be calculated as shown in Figs. 4(b–e) for different input states and loop directions. For verification, numerical simulations are also performed based on COMSOL Multiphysics, and the results are illustrated in Fig. 4, showing the excellent agreement with theoretical ones. Notice that the simulation model is similar to that illustrated in Figs. 3(b, c), except that the far side of the semi-infinite medium is terminated by the perfectly matched layer.

The variation of modal amplitudes in the process of dynamic encircling of the EP can be retrieved from the displacement fields based on the following method. The displacement $\mathbf{U}^{(n)}(\zeta_n)$ at the point of $\zeta = \zeta_n$ can be written in terms of the eigenvector of the n-th layer as

$$\mathbf{U}^{(n)}\left(\zeta_n\right) = q_{\text{L}}^{(n)}\boldsymbol{\Psi}_{\text{L}}^{(n)} + q_{\text{H}}^{(n)}\boldsymbol{\Psi}_{\text{H}}^{(n)} \tag{40}$$

where $q_{\text{L,H}}^{(n)}$ and $\boldsymbol{\Psi}_{\text{L,H}}^{(n)}$ denote modal amplitudes and eigenvectors of L and H modes. By multiplying $(\boldsymbol{\Psi}_{\text{L,H}}^{(n)})^{\text{T}}\mathbf{K}^{(n)}$ on both sides of Eq. (40), and using the orthogonality relationship $(\boldsymbol{\Psi}_{\text{L,H}}^{(n)})^{\text{T}}\mathbf{K}^{(n)}\boldsymbol{\Psi}_{\text{H,L}}^{(n)} = 0$ (Veletsos and Ventura, 1986), the modal amplitude $q_{\text{L,H}}^{(n)}$ can be determined as

$$q_{\text{L,H}}^{(n)} = \frac{\left(\boldsymbol{\Psi}_{\text{L,H}}^{(n)}\right)^{\text{T}}\mathbf{K}^{(n)}\mathbf{U}^{(n)}\left(\zeta_n\right)}{\left(\boldsymbol{\Psi}_{\text{L,H}}^{(n)}\right)^{\text{T}}\mathbf{K}^{(n)}\boldsymbol{\Psi}_{\text{L,H}}^{(n)}} \tag{41}$$

where $\mathbf{K}^{(n)}$ is the stiffness matrix as defined by Eq. (9). Fig. 5 shows the variation of modal amplitudes in the dynamic encircling of the PT-symmetric EP for different input states and evolution directions. There are two core signatures that significantly affect the dynamic evolution behavior. One performance is that the modal amplitude curve of L or H modes is subject to an abrupt change as caused by the branch cut (BC) line. Two modes exchange their identity when passing across this line. The other feature is the curve crossing phenomenon, which is inherently related to the non-adiabatic transition (NAT). The appearance of the NAT is required by the system stability, and it usually occurs when the high-loss mode dominates at the beginning of the evolution. Due to the joint action of the BC and NAT, the L (H) mode is dominant at the end of the evolution for the anti-clockwise (clockwise) evolution case, and the result is irrelevant to the input state, as confirmed by Fig. 5. This behavior is known as the chiral switching for the PT-symmetric phase.

Given the parametric trajectory (39), the evolution of modal amplitudes around the EP can be also predicted by the coupled-mode model (14). The displacement field $\tilde{\mathbf{U}}(\zeta)$ can be expressed as

$$\tilde{\mathbf{U}}(\zeta) = q_{\text{L}}(\zeta)\boldsymbol{\Psi}_{\text{L}}^{\text{TB}}(\zeta) + q_{\text{H}}(\zeta)\boldsymbol{\Psi}_{\text{H}}^{\text{TB}}(\zeta) \tag{42}$$

where $\boldsymbol{\Psi}_{\text{L,H}}^{\text{TB}}$ is the right eigenvector of the Hamiltonian matrix $\mathbf{H}_{\text{total}}(\zeta)$ as given by Eq. (15). Introduce the left eigenvector $\mathbf{I}_{\text{L,H}}^{\text{TB}}$, which can be calculated by using the relation $(\mathbf{H}_{\text{total}})^{\dagger}\mathbf{I}_{\text{L,H}}^{\text{TB}} = (\eta_{\text{L,H}}^{\text{TB}})^{*}\mathbf{I}_{\text{L,H}}^{\text{TB}}$. The left and right eigenvectors satisfy the bi-orthogonal

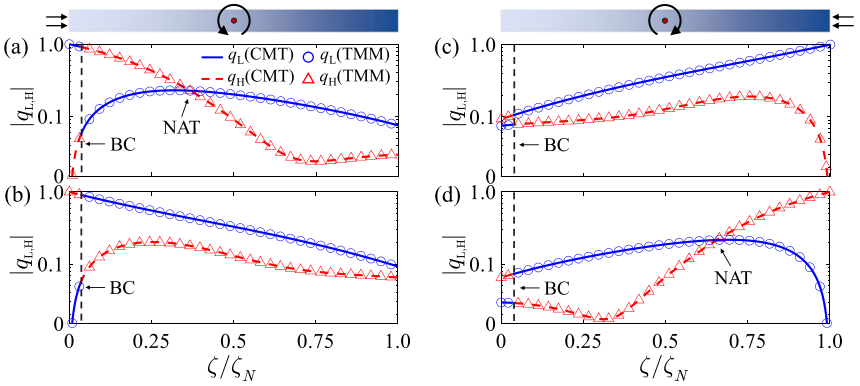

Fig. 5. Modal amplitudes in the process of dynamic encircling of the PT-symmetric EP calculated by the transfer-matrix method (TMM) and coupled-mode theory (CMT) in four cases: (a) the L mode and (b) H mode input for the anti-clockwise evolution; (c) the L mode and (d) H mode input for the clockwise evolution.

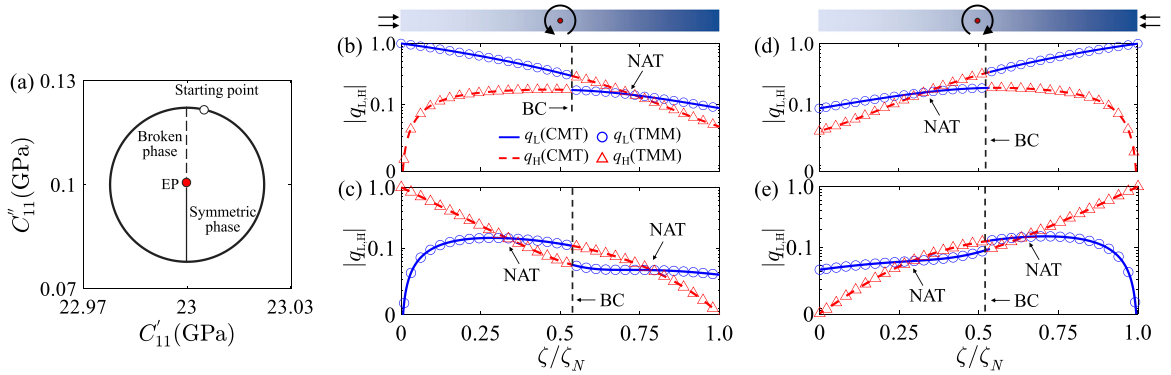

Fig. 6. (a) The circular loop trajectory same to Fig. 4(a) but with the starting point lying near the PT-broken phase, and (b–e) the corresponding modal amplitude results similar to those shown in Figs. 5(a–d).

relationship $(\mathbf{I}_i^{\mathrm{TB}})^\dagger \mathbf{\Psi}_j^{\mathrm{TB}} = \delta_{ij}$ $(i,j = \mathrm{L},\mathrm{H})$, where † denotes the conjugate transpose operation. By projecting the left eigenvectors $\mathbf{I}_{\mathrm{L,H}}^{\mathrm{TB}}(\zeta)$ onto the displacement field $\tilde{\mathbf{U}}(\zeta)$, the modal amplitude $q_{\mathrm{L,H}}$ can be calculated by

$$q_{\mathrm{L,H}}(\zeta) = \left[\mathbf{I}_{\mathrm{L,H}}^{\mathrm{TB}}(\zeta)\right]^\dagger \tilde{\mathbf{U}}(\zeta) \tag{43}$$

Results of modal amplitudes $q_{\mathrm{L,H}}$ calculated by the coupled-mode model have been plotted in Fig. 5, which coincide very well with those of transfer-matrix method, verifying the chiral transfer of the symmetric-phase mode.

Now study the dynamic encircling performance when the starting point lies at the vicinity of the PT-broken phase by setting $\phi_0 = 1.3\pi/3$, as sketched in Fig. 6(a). Figs. 6(b–e) show the variation of modal amplitudes for different starting states and evolution directions. When the L mode is excited, the system undergoes twice the mode switching caused by the BC and NAT respectively for both anticlockwise and clockwise encircling cases, and the output mode remains the same as the input state as indicated by Figs. 6(b, d). When the H mode is initially excited, it is finally converted to the L mode after experiencing twice NATs and once BC induced mode switching, as evidenced in Figs. 6(c, e). To conclude, the non-chiral mode switching behavior occurs when the starting point lies near the PT-broken phase, and the system always outputs the low-loss L mode irrelevant to input states and encircling directions, in accordance with the observation in optical (Zhang et al., 2018) and discrete mechanical systems (Geng et al., 2021b).

Chiral mode transfer is a manifestation of the Riemann surface topology, thus it is robust against not only the input state but also the loop trajectory. To demonstrate the latter effect, we devise an irregular loop trajectory as displayed in Fig. 7(a), which is parameterized by

$$\begin{cases} C'_{11}(\zeta) = 0.02 \times \left[2\cos\left(\omega_r\zeta - 0.6\pi\right) - \cos\left(2\omega_r\zeta - 0.6\pi\right)\right] + 23 \quad \text{(GPa)} \\ C''_{11}(\zeta) = 0.02 \times \left[2\sin\left(\omega_r\zeta - 0.6\pi\right) - \sin\left(2\omega_r\zeta - 0.6\pi\right)\right] + 0.1 \quad \text{(GPa)} \end{cases} \tag{44}$$

Modal amplitudes $q_{\mathrm{L,H}}$ calculated by the transfer matrix method and coupled-mode model are shown in Figs. 7(b–e) in four cases of different input states and evolution directions. Results show again the chiral behavior of mode switching, demonstrating its robustness against the shape change of the loop enclosing the EP. While preserving the chiral behavior, the shape change of the

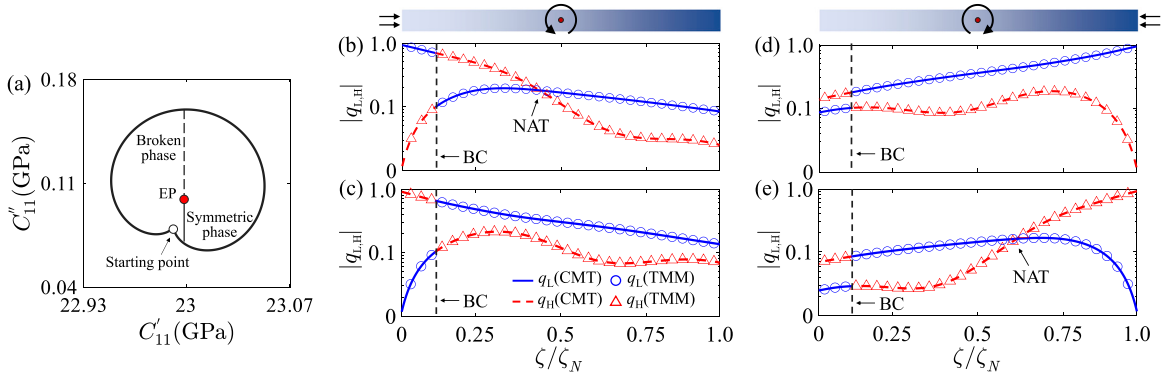

Fig. 7. (a) The irregular loop trajectory in the parameter space (C'_{11}, C''_{11}) used for implementing the dynamic encircling of the PT-symmetric EP; (b–e) Results similar to those shown in Figs. 5(a–d), but for a parametric loop along the irregular trajectory in (a).

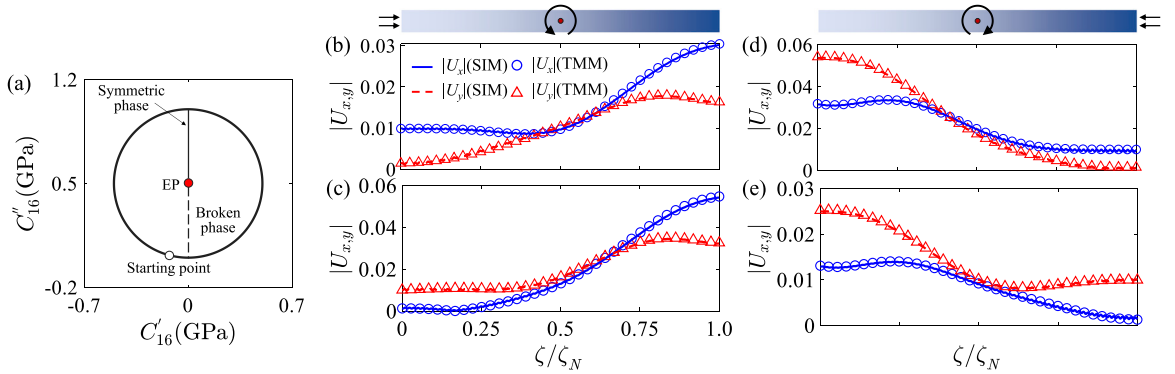

Fig. 8. (a) The circular loop trajectory in the parameter space (C'_{16}, C''_{16}) used for implementing the dynamic encircling of the anti-PT-symmetric EP with the starting point lying near the symmetry-broken phase; Normalized displacement amplitudes in the process of dynamic encircling of the anti-PT-symmetric EP calculated by the transfer-matrix method (TMM) and numerical simulation (SIM) in four cases: (b) the U mode and (c) B mode input for the anti-clockwise evolution; (d) the U mode and (e) B mode input for the clockwise evolution.

loop trajectory is found to have an enlargement effect on the amplitude ratio of output modes at the end of evolution. Thereby, the design of loop paths can act as a new degree for precise control of the chiral mode transfer.

3.3. Dynamic encircling of the anti-PT-symmetric EP

The dynamic encircling of the anti-PT-symmetric EP is implemented by choosing the parametric trajectory

$$\begin{cases} C'_{16}(\zeta) = 0.4\cos\left(\omega_r\zeta + \psi_0\right) & \text{(GPa)} \\ C''_{16}(\zeta) = 0.4\sin\left(\omega_r\zeta + \psi_0\right) + 0.5 & \text{(GPa)} \end{cases} \tag{45}$$

where $\omega_r = 2\pi/L_t$, $L_t = Nk_s w$, $N = 540$, and $w = 29.4$ mm. The modulus $C_{16}^{(n)}$ of the n-th layer is given by $C_{16}(L_n)$, where $L_n = (n-1)k_s w$. The parametric loop defined by Eq. (45) is displayed in Fig. 8(a), where the starting point is set near the symmetry-broken phase by choosing $\psi_0 = -1.7\pi/3$. The modulus properties of the semi-infinite medium are set as $C_{11} = 24$ GPa, $C_{66} = 23$ GPa, $C_{16} = 0$ according to the same rule as explained in PT-symmetric systems. Based on the transfer matrix method, the displacement fields in the multilayered structure can be calculated by solving Eq. (31), and then used to retrieve the modal amplitudes based on Eq. (41). For brevity, the upper and bottom spectrum sheets of $\mathrm{Re}(\eta_\pm)$ in Fig. 2 are termed as the U and B modes, respectively. Theoretical results of displacement fields are calculated for different input states and loop directions as shown in Figs. 8(b–e), which are in good agreement with simulation results.

Fig. 9 plots the modal amplitude curves of U and B modes in the dynamic encircling of the anti-PT-symmetric EP for different input states and loop directions. In the anti-clockwise evolution case, the U mode is dominant at the end of the evolution, while the system outputs the B mode in the clockwise evolution case. Above behavior is irrelevant to input states, demonstrating the chiral conversion of symmetry-broken states. Figs. 10(b–e) display the mode evolution results when the starting point lies near the anti-PT-symmetric phase by setting $\psi_0 = 1.3\pi/3$, as sketched in Fig. 10(a). It is found that the system always outputs the U mode irrelevant to the input mode and encircling direction, showcasing the non-chiral mode conversion behavior.

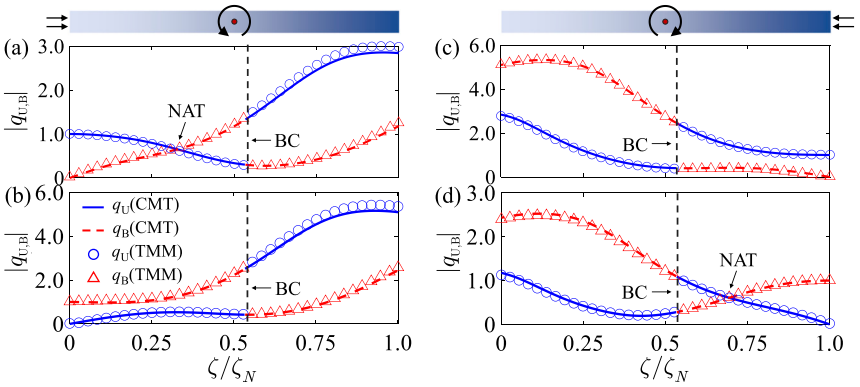

Fig. 9. Modal amplitudes in the process of dynamic encircling of the anti-PT-symmetric EP calculated by the transfer-matrix method (TMM) and coupled-mode theory (CMT) in four cases: (a) the U mode and (b) B mode input for the anti-clockwise evolution; (c) the U mode and (d) B mode input for the clockwise evolution.

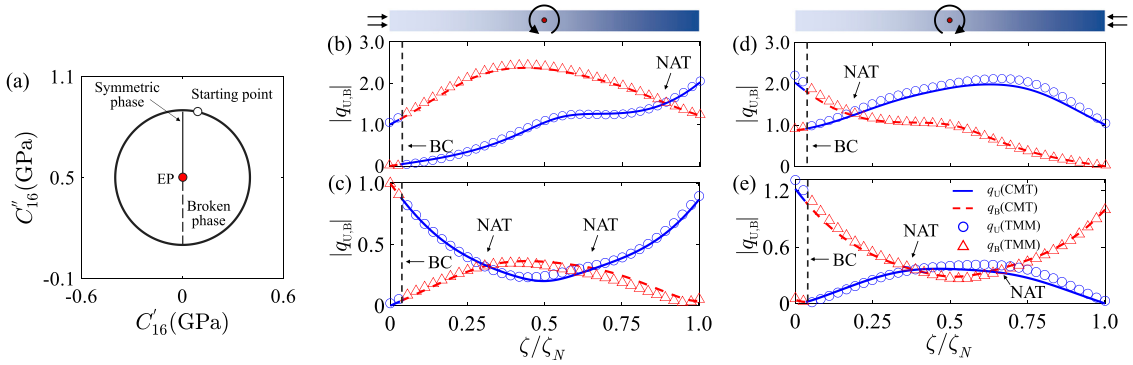

Fig. 10. (a) The circular loop trajectory same to Fig. 8(a) but with the starting point lying near the anti-PT-symmetric phase, and (b–e) the corresponding modal amplitude results similar to those shown in Figs. 9(a–d).

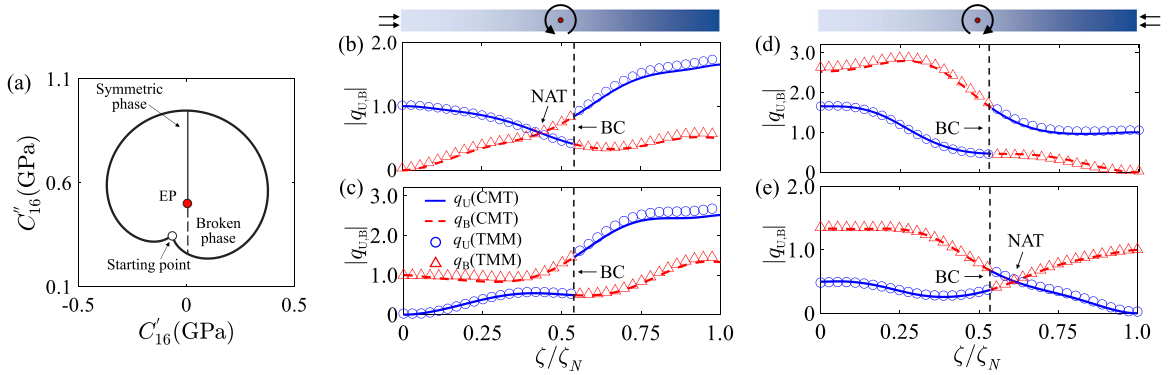

Fig. 11. (a) The irregular loop trajectory in the parameter space (C'_{16}, C''_{16}) used for implementing the dynamic encircling of the anti-PT-symmetric EP; (b–e) Results similar to those shown in Figs. 9(a–d), but for a parametric loop along the irregular trajectory in (a).

The chiral behavior of the broken phase is further studied by postulating an irregular loop trajectory as drawn in Fig. 11(a), which is defined by

$$\begin{cases} C'_{16}(\zeta) = 0.15 \times \left[2\cos\left(\omega_r\zeta - 0.6\pi\right) - \cos\left(2\omega_r\zeta - 0.6\pi\right)\right] & \text{(GPa)} \\ C''_{16}(\zeta) = 0.15 \times \left[2\sin\left(\omega_r\zeta - 0.6\pi\right) - \sin\left(2\omega_r\zeta - 0.6\pi\right)\right] + 0.5 & \text{(GPa)} \end{cases} \tag{46}$$

Results of modal amplitudes of U and B modes are illustrated in Figs. 11(b–e), proving again the chiral transfer of the broken phase and its robustness against the shape change of the loop enclosing the EP.

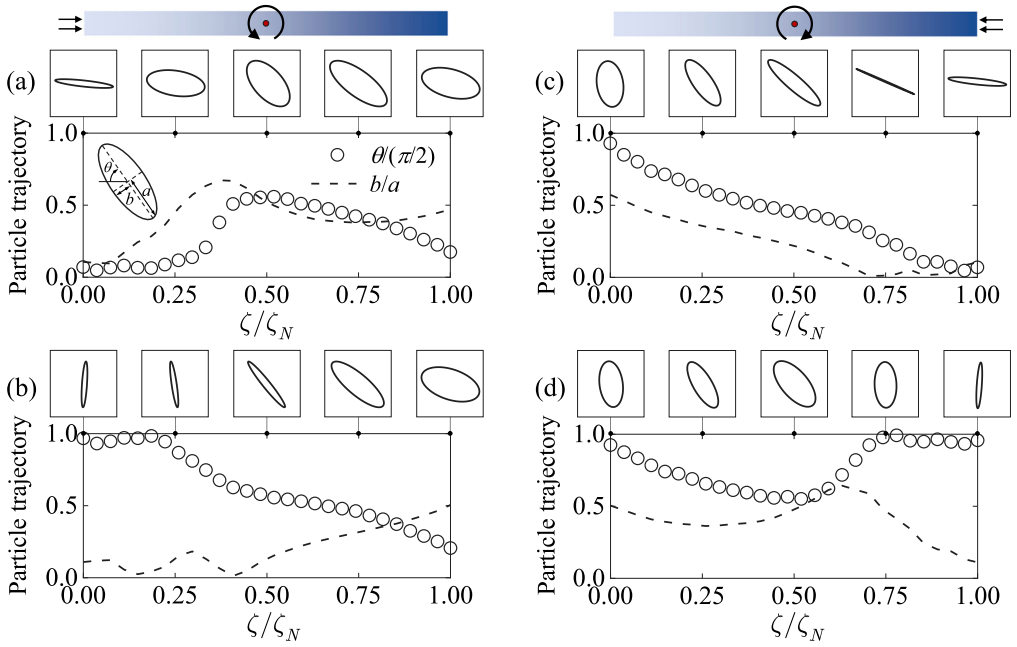

Fig. 12. (a–d) The orientation angle (θ) and aspect ratio (b/a) of trajectory ellipse for each particle in the multilayer structure, corresponding to four cases in Figs. 8(b–e) respectively.

According to Fig. 2(f), the U and B modes near the broken phase are characterized by the quasi-longitudinal (QL) and quasi-transverse (QT) polarization features. Therefore, the chiral dynamics of the broken phase may provide a new mechanism for unusual mode conversion of classical elastic P and S waves. By taking the circular loop encircling case in Fig. 8 as an example, further analyses are given here regarding the wave polarization evolution as the incident wave propagates through the multilayer structure. According to displacement fields in Fig. 8, the motion trajectory of particles is found to follow the elliptic profile. Therefore, the polarization evolution can be characterized by the ellipse orientation angle (θ) and aspect ratio (b/a) as shown in Fig. 12, corresponding to four cases in Figs. 8(b–e) respectively. It is seen from Fig. 12(a) that, when the U mode with the QL feature is inputted from the left, the orientation angle varies at different positions as the wave propagates, and remains the nearly longitudinal polarization at the exit port. While for the rightward input case in Fig. 12(c), the U mode is eventually converted to the transverse motion. By contrast, the B mode undergoes the polarization conversion in the leftward incidence case as shown in Fig. 12(b), while still keeping the QT feature when the wave is incident from the right as displayed in Fig. 12(d). The orientation angle evolution clearly demonstrates the polarization conversion functionality for elastic waves, and the underlying mechanism can be attributed to the chiral dynamics of the broken phase. In all cases, the aspect ratio of trajectory ellipse at exit ports is not perfect, namely not sufficiently small. The reason can be understood from the modal amplitude curves in Fig. 9, where the modal amplitude of the non-dominant output state is not vanishingly small. It is worth noting that the amplitude ratio between two states at the output port is affected by the loop shape and evolution rate. Therefore, the mode purity at exit ports can be improved by optimization design of the path enclosing the EP.

The mode conversion efficiency measures the fraction of energy transformed from an input mode to a different target output mode (Yang and Kim, 2018). Thanks to the gain feature of anti-PT-symmetric system, the energy of the desired output mode can be significantly enhanced relative to the input energy with the conversion efficiency beyond unity as observed in Fig. 9. The modal amplitude ratio between the input U (B) mode and output B (U) mode can reach up to 5.11 (5.36), showcasing the superior mode conversion efficiency. It is worth noting that the mode conversion based on the chiral dynamics can possess the topological robustness against the imperfection of propagation medium, as confirmed in Figs. 9 and 11 where the chiral mode conversion is available for both regular and irregular loop trajectories. This acts as a unique feature compared with other mode conversion mechanisms (Zhu et al., 2014; Yang and Kim, 2018; Wei et al., 2024).

4. Conclusions

Elastic media with anisotropic elasticity involve rich polarization modes and strong mode couplings, which make them an ideal platform to explore the non-Hermitian behavior for elastic waves. In this work, the PT-symmetric/anti-PT-symmetric EPs and chiral mode conversion of elastic waves via the dynamic encircling of them are realized in anisotropic elastic media with complex modulus. Based on the tight-binding approximation, the elastodynamic equation of 2D anisotropic media is formulated as the form of the Schrödinger-like equation with the non-Hermitian Hamiltonian. The eigenvalue analyses of the Hamiltonian disclose the existence of

the PT and anti-PT symmetry, and derive the parameter conditions for the appearance of EPs. The dynamic evolution of eigenmodes encircling the EP is implemented in the multilayered structure, where each layered medium corresponds to a discretized parametric point in the loop enclosing the EP. Based on the transfer matrix method, the displacement fields in the multilayered structure are analytically calculated, and used to retrieve the variation of modal amplitudes in the process of dynamic encircling of the EP. The dynamic evolution of eigenmodes is studied in different cases of input states and loop directions. It is found that the dynamical encircling of a PT-symmetric EP can lead to chiral transfer for the PT-symmetric phase, while the encircling of an anti-PT-symmetric EP results in chiral switching for the symmetry-broken phase. The chiral behavior is decided primarily by the loop direction, and is robust against not only the input state but also the shape change of the loop trajectory.

In our study, the PT-symmetric elastic medium is a purely lossy system without requiring the energy gain. A desirable option for its practical realization is based on the composite material embedded with ferromagnetic/ferroelectric particles, which are driven by external magnetic/electric fields (Borin and Stepanov, 2015). The constitutive relation of the composite material can be described by viscoelastic properties with storage modulus and loss modulus, which jointly generates the complex elastic modulus. These modulus properties can be flexibly tuned by modulating the intensity of applied magnetic/electric field. By contrast, the designed anti-PT-symmetric elastic medium requires the gain effect, and an ideal candidate for its practical realization is based on composite piezoelectric structures with the shunting circuit (Singh et al., 2021, 2022). The circuit system can provide a large degree to customize the gain/loss property of complex elastic modulus by means of shunting circuits (Chen et al., 2017; Li et al., 2018; Zhu et al., 2016; Thomes et al., 2024) or active feedback transfer function control (Liu et al., 2024). Therefore, the designed non-Hermitian elastic media are physically realizable in experimental platform. The proposed studies may open a new avenue towards unusual propagation and polarization control for elastic waves.

CRediT authorship contribution statement

Youdong Duan: Writing – original draft, Methodology, Investigation, Formal analysis, Conceptualization. **Linlin Geng:** Validation, Investigation. **Guoliang Huang:** Writing – review & editing, Validation, Investigation. **Xiaoming Zhou:** Writing – review & editing, Validation, Supervision, Methodology, Conceptualization.

Declaration of competing interest

The authors declare that they have no known competing financial interests or personal relationships that could have appeared to influence the work reported in this paper.

Acknowledgments

This work was supported by the National Natural Science Foundation of China (12225203, 11622215, 11872111, 11991030, and 11991033), and the 111 Project (B16003).

Data availability

Data will be made available on request.

References

Borin, D.Y., Stepanov, G.V., 2015. Elastomer with magneto- and electrorheological properties. J. Intell. Mater. Syst. Struct. 26 (14), 1893–1898.
Cai, R., Jin, Y., Li, Y., Rabczuk, T., Pennec, Y., Djafari-Rouhani, B., Zhuang, X., 2022. Exceptional points and skin modes in non-Hermitian metabeams. Phys. Rev. Appl. 18 (1), 014067.
Cai, R., Jin, Y., Li, Y., Zhu, J., Zhu, H., Rabczuk, T., Zhuang, X., 2023. Absorption-lasing effects and exceptional points in parity-time symmetric non-Hermitian metaplates. J. Sound Vibr. 555, 117710.
Chen, Y., Hu, G., Huang, G., 2017. A hybrid elastic metamaterial with negative mass density and tunable bending stiffness. J. Mech. Phys. Solids. 105, 179–198.
Chen, Y., Li, X., Scheibner, C., Vitelli, V., Huang, G., 2021. Realization of active metamaterials with odd micropolar elasticity. Nat. Commun. 12 (1), 5935.
Christensen, J., Haberman, M.R., Srivastava, A., Huang, G., Shmuel, G., 2024. Perspective on non-Hermitian elastodynamics. Appl. Phys. Lett. 125 (23), 230501.
Dembowski, C., Dietz, B., Gräf, H., Harney, H., Heine, A., Heiss, W., Richter, A., 2004. Encircling an exceptional point. Phys. Rev. E 69 (5), 056216.
Dembowski, C., Gräf, H., Harney, H., Heine, A., Heiss, W., Rehfeld, H., Richter, A., 2001. Experimental observation of the topological structure of exceptional points. Phys. Rev. Lett. 86 (5), 787–790.
Ding, K., Fang, C., Ma, G., 2022. Non-Hermitian topology and exceptional-point geometries. Nat. Rev. Phys. 4 (12), 745–760.
Ding, K., Ma, G., Xiao, M., Zhang, Z.Q., Chan, C.T., 2016. Emergence, coalescence, and topological properties of multiple exceptional points and their experimental realization. Phys. Rev. X 6 (2), 021007.
Ding, K., Ma, G., Zhang, Z.Q., Chan, C.T., 2018. Experimental demonstration of an anisotropic exceptional point. Phys. Rev. Lett. 121 (8), 085702.
Duan, Y., Geng, L., Guo, Q., Yang, J., Hu, G., Zhou, X., 2023. Acoustic chiral mode switching by dynamic encircling of exceptional points. Appl. Phys. Lett. 123 (10), 101701.
Duan, Y., Zhang, L., Zhang, Y., Geng, L., Guo, Q., Yang, J., Hu, G., Zhou, X., 2024. Acoustic chiral mode transfer for symmetry-broken states in anti-parity-time symmetric systems. Extrem. Mech. Lett. 73, 102261.
Elbaz, G., Pick, A., Moiseyev, N., Shmuel, G., 2022. Encircling exceptional points of Bloch waves: mode conversion and anomalous scattering. J. Phys. D-Appl. Phys. 55 (23), 235301.
Feng, Z., Sun, X., 2022. Harnessing dynamical encircling of an exceptional point in anti-PT-symmetric integrated photonic systems. Phys. Rev. Lett. 129 (27), 273601.

Fishman, A., Elbaz, G., Varma, T.V., Shmuel, G., 2024. Third-order exceptional points and frozen modes in planar elastic laminates. J. Mech. Phys. Solids. 186, 105590.
Fleury, R., Sounas, D., Alu, A., 2015. An invisible acoustic sensor based on parity-time symmetry. Nat. Commun. 6, 5905.
Gao, T., Estrecho, E., Bliokh, K.Y., Liew, T.C.H., Fraser, M.D., Brodbeck, S., Kamp, M., Schneider, C., Hoefling, S., Yamamoto, Y., Nori, F., Kivshar, Y.S., Truscott, A.G., Dall, R.G., Ostrovskaya, E.A., 2015. Observation of non-Hermitian degeneracies in a chaotic exciton-polariton billiard. Nat. 526 (7574), 554–558.
Gao, P., Qu, Y., Christensen, J., 2022. Non-Hermitian elastodynamics in gyro-odd continuum media. Commun. Mater. 3 (1), 74.
Geng, L., Zhang, W., Zhang, X., Zhou, X., 2021a. Chiral mode transfer of symmetry-broken states in anti-parity-time-symmetric mechanical system. Proc. R. Soc. A-Math. Phys. Eng. Sci. 477 (2256), 20210641.
Geng, L., Zhang, W., Zhang, X., Zhou, X., 2021b. Topological mode switching in modulated structures with dynamic encircling of an exceptional point. Proc. R. Soc. A-Math. Phys. Eng. Sci. 477 (2245), 20200766.
Gu, Z., Gao, H., Cao, P.-C., Liu, T., Zhu, X.-F., Zhu, J., 2021. Controlling sound in non-Hermitian acoustic systems. Phys. Rev. Appl. 16 (5), 057001.
Harrison, W., 1994. Tight-binding methods. Surf. Sci. 299, 298–310.
Jin, Y., Li, W., Djafari-Rouhani, B., Li, Y., Xiang, Y., 2024. Exceptional points for crack detection in non-Hermitian beams. J. Sound Vibr. 572, 118162.
Koutserimpas, T.T., Fleury, R., 2020. Electromagnetic fields in a time-varying medium: exceptional points and operator symmetries. IEEE Trans. Antennas Propag. 68 (9), 6717–6724.
Li, X., Chen, Y., Hu, G., Huang, G., 2018. A self-adaptive metamaterial beam with digitally controlled resonators for subwavelength broadband flexural wave attenuation. Smart Mater. Struct. 27 (4), 045015.
Li, A., Dong, J., Wang, J., Cheng, Z., Ho, J.S., Zhang, D., Wen, J., Zhang, X.-L., Chan, C.T., Alu, A., Qiu, C.-W., Chen, L., 2020. Hamiltonian hopping for efficient chiral mode switching in encircling exceptional points. Phys. Rev. Lett. 125 (18), 187403.
Li, P.-H., Wang, Y.-Z., 2023. Negative refraction and exceptional point with parity-time symmetry in a piezoelectric mechanical metamaterial. Mech. Mater. 181, 104647.
Li, A., Wei, H., Cotrufo, M., Chen, W., Mann, S., Ni, X., Xu, B., Chen, J., Wang, J., Fan, S., Qiu, C.-W., Alu, A., Chen, L., 2023. Exceptional points and non-Hermitian photonics at the nanoscale. Nat. Nanotechnol. 18 (7), 706–720.
Liu, Q., Liu, J., Zhao, D., Wang, B., 2021a. On-chip experiment for chiral mode transfer without enclosing an exceptional point. Phys. Rev. A 103 (2), 023531.
Liu, W., Wu, Y., Duan, C.-K., Rong, X., Du, J., 2021b. Dynamically encircling an exceptional point in a real quantum system. Phys. Rev. Lett. 126 (17), 170506.
Liu, Z., Yi, K., Sun, H., Zhu, R., Zhou, X., Hu, G., Huang, G., 2024. Inherent temporal metamaterials with unique time-varying stiffness and damping. Adv. Sci. 11 (43), 2404695.
Liu, W., Zhang, Y., Deng, Z., Ye, J., Wang, K., Wang, B., Gao, D., Lu, P., 2022. On-chip chiral mode switching by encircling an exceptional point in an anti-parity-time symmetric system. Laser Photon. Rev. 16 (12), 2100675.
Naghiloo, M., Abbasi, M., Joglekar, Y.N., Murch, K.W., 2019. Quantum state tomography across the exceptional point in a single dissipative qubit. Nat. Phys. 15 (12), 1232–1236.
Nassar, H., Xu, X.C., Norris, A.N., Huang, G.L., 2017. Modulated phononic crystals: Non-reciprocal wave propagation and willis materials. J. Mech. Phys. Solids. 101, 10–29.
Nassar, H., Yousefzadeh, B., Fleury, R., Ruzzene, M., Alu, A., Daraio, C., Norris, A.N., Huang, G., Haberman, M.R., 2020. Nonreciprocity in acoustic and elastic materials. Nat. Rev. Mater. 5 (9), 667–685.
Ozdemir, S.K., Rotter, S., Nori, F., Yang, L., 2019. Parity-time symmetry and exceptional points in photonics. Nat. Mater. 18 (8), 783–798.
Singh, A., Mukhopadhyay, T., Adhikari, S., Bhattacharya, B., 2021. Voltage-dependent modulation of elastic moduli in lattice metamaterials: Emergence of a programmable state-transition capability. Int. J. Solids Struct. 208, 31–48.
Singh, A., Mukhopadhyay, T., Adhikari, S., Bhattacharya, B., 2022. Active multi-physical modulation of Poisson's ratios in composite piezoelectric lattices: On-demand sign reversal. Compos. Struct. 280, 114857.
Tang, W., Jiang, X., Ding, K., Xiao, Y.-X., Zhang, Z.-Q., Chan, C.T., Ma, G., 2020. Exceptional nexus with a hybrid topological invariant. Sci. 370 (6520), 1077–1080.
Thomes, R.L., Rosa, M.I.N., Erturk, A., 2024. Experimental realization of tunable exceptional points in a resonant non-Hermitian piezoelectrically coupled waveguide. Appl. Phys. Lett. 124 (6), 061702.
Torrent, D., Parnell, W.J., Norris, A.N., 2018. Loss compensation in time-dependent elastic metamaterials. Phys. Rev. B 97 (1), 014105.
Veletsos, A., Ventura, C., 1986. Modal analysis of non-classically damped linear systems. Earthq. Eng. Struct. Dyn. 14 (2), 217–243.
Wei, Y., Cai, M., Hu, G., 2024. Elastic birefringent metamaterials and quarter-wave plate. Int. J. Mech. Sci. 281, 109684.
Wei, Y., Zhou, H., Chen, Y., Ding, Y., Dong, J., Zhang, X., 2022. Anti-parity-time symmetry enabled on-chip chiral polarizer. Photonics Res. 10 (1), 76–83.
Wu, Q., Chen, Y., Huang, G., 2019. Asymmetric scattering of flexural waves in a parity-time symmetric metamaterial beam. J. Acoust. Soc. Am. 146 (1), 850–862.
Wu, Q., Wang, S., Qian, H., Wang, Y., Huang, G., 2024. Understanding of topological mode and skin mode morphing in 1D and 2D non-Hermitian resonance-based meta-lattices. J. Mech. Phys. Solids. 193, 105907.
Wu, Q., Xu, X., Qian, H., Wang, S., Zhu, R., Yan, Z., Ma, H., Chen, Y., Huang, G., 2023. Active metamaterials for realizing odd mass density. Proc. Natl. Acad. Sci. U. S. A. 120 (21), e2209829120.
Xing, T., Pan, Z., Tao, Y., Xing, G., Wang, R., Liu, W., Xing, E., Rong, J., Tang, J., Liu, J., 2020. Ultrahigh sensitivity stress sensing method near the exceptional point of parity-time symmetric systems. J. Phys. D-Appl. Phys. 53 (20), 205102.
Yang, X., Kim, Y.Y., 2018. Asymptotic theory of bimodal quarter-wave impedance matching for full mode-converting transmission. Phys. Rev. B 98 (14), 144110.
Yang, F., Liu, Y.-C., You, L., 2017. Anti-PT symmetry in dissipatively coupled optical systems. Phys. Rev. A 96 (5), 053845.
Yuan, J., Geng, L., Huang, J., Guo, Q., Yang, J., Hu, G., Zhou, X., 2022. Exceptional points induced by time-varying mass to enhance the sensitivity of defect detection. Phys. Rev. Appl. 18 (6), 064055.
Zhang, X.-L., Jiang, T., Chan, C.T., 2019. Dynamically encircling an exceptional point in anti-parity-time symmetric systems: asymmetric mode switching for symmetry-broken modes. Light-Sci. Appl. 8, 88.
Zhang, X.-L., Wang, S., Hou, B., Chan, C.T., 2018. Dynamically encircling exceptional points: In situ control of encircling loops and the role of the starting point. Phys. Rev. X 8 (2), 021066.
Zhu, R., Chen, Y.Y., Barnhart, M.V., Hu, G.K., Sun, C.T., Huang, G.L., 2016. Experimental study of an adaptive elastic metamaterial controlled by electric circuits. Appl. Phys. Lett. 108 (1), 011905.
Zhu, R., Liu, X.N., Hu, G.K., Sun, C.T., Huang, G.L., 2014. Negative refraction of elastic waves at the deep-subwavelength scale in a single-phase metamaterial. Nat. Commun. 5, 5510.